




Studies on structural, dielectric behavior, and electrical properties of BiBaNiNbO₆ double perovskite for electronic applications

K. Iben Nassar^{1,*} , F. Tayari¹, M. Slimi^{1,2}, N. Rammeh¹, A. Njeh¹, S. Soreto Teixeira³, and M. P. F. Graça³

¹Laboratoire de physique des materiaux, Faculté des Sciences de Sfax, Université de Sfax, B.P. 1171, 3000 Sfax, Tunisia

²Faculté des Sciences de Monastir, Université de Monastir, 5019 Monastir, Tunisia

³IN-Aveiro, Department of Physics, University of Aveiro, 3810-193 Aveiro, Portugal

Received: 9 August 2022

Accepted: 17 October 2022

Published online:

4 November 2022

© The Author(s), under exclusive licence to Springer Science+Business Media, LLC, part of Springer Nature 2022

ABSTRACT

The structural, morphological, dielectric and electrical properties for BiBaNiNbO₆ sample prepared by sol–gel method have been investigated in this work. X-ray investigation confirms the formation of single phase with rhombohedral crystal structure with space group $R\bar{3}C$ at room temperature. Energy dispersion spectroscopy (EDS) analysis and scanning electron microscopy were used to confirm the chemical make-up of the synthesized molecule and the morphology of the grain size (SEM). The $Z''(f)$ curve confirms the appearance of a relaxation phenomenon in the sample which exhibits semiconductor behavior. An electrical circuit consisting of a link of grain and grain boundary elements is used to analyze the Nyquist plots between the ranges of 200 and 360 K and 100 Hz and 1 MHz, respectively. The variation of electrical conductivity at various temperatures obeys the Jonscher's power law. The Non-overlapping Small Polaron Tunneling (NSPT) is the appropriate model to explain the conduction mechanism for the sample. The estimated activation energies from the DC conductivity and electrical impedance are close implying that the relaxation and conduction processes are caused by the same type of charge carriers. Electrical and optical properties show higher electrical resistivity and considerable visible light absorption which makes the prepared BiBaNiNbO₆ double perovskite suitable candidate for electrical applications.

Address correspondence to E-mail: Kaisibnnassar12@gmail.com

1 Introduction

The perovskite group of ceramic materials is the most generally appearing and significant in materials science and has been broadly analysed in the recent years. Various writers have extensively examined and investigated substances that crystallize in the perovskite structure in both physics and solid-state chemistry [1–3]. Physical characteristics of most of perovskite have huge significance in microelectronics and telecommunication [4]. It is well-known that structural distortions, vacancies and compositional modifications can induce a great variety of physical and chemical properties [5]. When the ideal perovskite structure of general formula ABO_3 is modified to introduce two different types of cations on the octahedral site of the primitive unit cell perovskite, the cationic order leads to a complex cubic perovskite superstructure called double perovskite of general stoichiometry $A'A''B'B''O_6$ [6]. Where, the cations occupying the A' and A'' site of the perovskite are essentially alkaline earth metal ions or rare earth, while the cations occupying the site B' and B'' are two different transition metals surrounded by the oxygen anions thus forming octahedral $B'O_6$ and $B''O_6$ joined by the vertices.

Oxide materials are the subject of much research. There are many researches have been conducted on physical, electrical, dielectric and magnetic properties, due to their technological applications in industry as catalyst, magnetic recording, in the field of microelectronics, energy storage [7–12], magnetic memory components, electrode and electrolyte materials for fuel cells [13], and solar cell components [14]. In addition, for magnetic properties, these types of compounds are used in electronic devices, magnetic resonance imaging (MRI), hyperthermia, information storage and drug delivery [15, 16]. Moreover, the perovskite oxides have different crystal structures such as cubic, for example $LaBa_{0.5}Ag_{0.5}FeMnO_6$ [17] and $La_{1-x}Li_xSrMn_2O_{5+\delta}$ ($x = 0.05, 0.10$ and 0.15) [18], rhombohedral system, namely the compound $LaPbFeTiO_6$ [19] and $BiBaFeZnO_6$ [20], tetragonal ($I4/m$) such as the Sr_2CoWO_6 [21] and monoclinic ($P2_1/n$) as an example Ca_2FeMoO_6 [22].

Besides, the combinations of ions of ions at sites A and B with different ionic sizes and valences in the double perovskite formula $A_2B'B''O_6$, leading to very different physical and chemical properties. They can also have different electronic behaviors, ranging from

insulator to metallic, with spin-polarized electrical conductivity [23, 24], as well as ferroic atomic shifts [25] and ionic conductivity [26]. In the literature, the $BiBaFeZnO_6$ sample was synthesized by the sol–gel method. The structural study shows that the sample is monophasic and crystallizes in the rhombohedral system with the space group the $R\bar{3}C$. Their dielectric and electrical properties have been studied using the complex impedance technique. Thus, this material is of interest for the future in technological applications. However, the studied sample shows that the variation of the electric conductivity indicates a semiconductor character; it also shows the presence of a phenomenon of dielectric relaxation and conduction [20].

In this work, a systematic study of dielectric, impedance and conductivity of polycrystalline compound $BiBaNiNbO_6$ (BNO) is presented in the temperature range of 200–360 K and frequency range of 100 Hz to 1 MHz. One of the objectives was to prepare this double perovskite material by the sol–gel method. Also, we have studied in detail its structural, morphological and chemical properties by X-ray diffraction and scanning electron microscopy, the dielectric and electrical properties using the method of complex impedance spectroscopy. Moreover, the study of dielectric properties is one of the most important areas of materials science. It concerns the storage and dissipation of electrical and magnetic energy in materials. They are important in explaining various phenomena in electronics, optics and solid-state physics. Therefore, our material presents interesting dielectric properties because it has a high permittivity. It is used as a capacitor to store energy. On the other hand, in a transformer, the dielectric material is used as an insulator and a cooling agent. To improve the performance of a semiconductor device, high permittivity dielectric materials are used.

2 Experimental details

2.1 Sample preparation

We have prepared the nanoparticles perovskite oxide with nominal composition $BiBaNiNbO_6$ by sol–gel method using stoichiometric amounts of precursors, bismuth nitrate $Bi(NO_3)_3 \cdot 5H_2O$, barium carbonate $BaCO_3$, oxide nickel NiO and oxide niobium Nb_2O_5 .

Our sample is synthesized from high purity precursors (99.9%). The various precursors were dissolved in nitric acid and water distilled at 120 °C for 4 h with stirring magnetic mixer. Then, citric acid and ethylene glycol are added. The obtained solution was dried and calcined to obtain a nano-crystalline powder. The material was crushed and pressed into a pellet and then sintered. Finally, it was annealed between 600 and 900 °C for 12 h to obtain a homogeneous material.

2.2 Characterization technique

Several experimental techniques were used in order to characterize and identify our compound. The crystallinity, crystal structure, crystal phase analysis of the BiBaNiNbO₆ compound were studied by X-ray diffraction (XRD) technique using Cu-K α 1 radiation ($\lambda = 1.54056 \text{ \AA}$), using an X'Pert MPD Philips diffractometer was performed at room temperature. Morphology of the sample was analyzed by scanning electron microscopy (SEM), using a TESCAN Vega 3 microscope. The nanoparticles were suspended on carbon coated copper grid by dropping a drop of dispersion. Temperature dependent dielectric and electrical properties of the sample were studied by impedance spectroscopy complex (ISC). Measurements of these properties were conducted using a precision impedance analyzer, Agilent 4294A, in the C_p-R_p configuration (capacitance in parallel with resistance), in a frequency range of 100 Hz to 1 MHz and temperature range of 200–380 K using a bath cryostat. The sample was put in a helium atmosphere to improve the heat transfer and avoid moisture. Besides, the compounds were used in the used disk form, with the opposite surfaces painted with conductive silver paste, to the electrodes.

3 Results and discussion

3.1 Characterization by X-ray diffraction

The X-ray powder diffracton (XRD) profile of the synthesized BiBaNiNbO₆ powder was shown in the Fig. 1 at room temperature. The diffraction peaks were generated by X-ray scattering from well crystallined lattice. Hence the prepared BNO was well crystallined compound. The structure refinement was recorded using the Rietveld [27–29] method and the

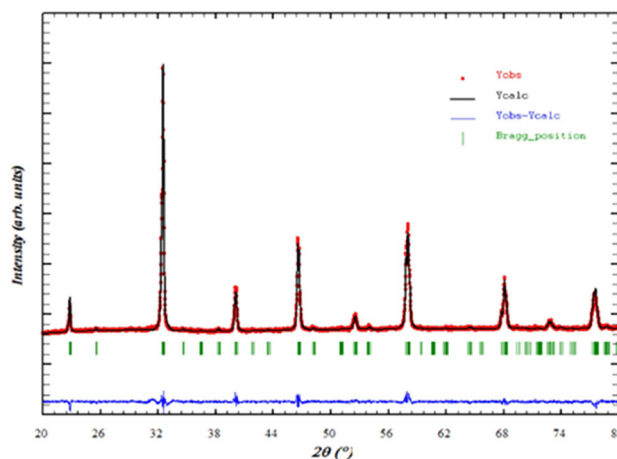


Fig. 1 (a) SEM of the studied sample, (b) chemical analysis EDX

Fullprof program [30–32]. Further, no supplemental peaks corresponding to other secondary phases were observed from the XRD pattern indicating the good crystallization of the synthesized sample. The figure shows that pure sample and crystallizes in the rhombohedral system with the space group $R\bar{3}C$ and that there is agreement between the calculated and measured intensities. Table 1 summarized the results of the Rietveld refinement, which describes the cell parameters and the angles, the dependability factors χ^2 , Bragg factor R_B , and bond lengths.

The average crystallite size of the compound was estimated from the full width at half-maxima (FWHM) of the peak profile distribution fitted to Pseudo Voigt function. The average crystallite (D_{SC}) of the sample was estimated by the following Scherrer equation [33, 34]:

$$D_{SC} = \frac{0.9 \cdot \lambda}{\beta \cdot \cos \theta} \quad (1)$$

Table 1 Structural parameters, angles and bond lengths obtained through refinement of BiBaNiNbO₆

Sample	BiBaNiNbO ₆
$a = b$ (Å)	5.5431
c (Å)	13.5851
V (Å ³)	364.4470
χ^2	1.38
R_f	1.46
R_B	1.86
$\alpha = \beta$ (°)	90°
γ (°)	120°
Nb–O (Å)	2.1578
Ni–O (Å)	1.8386
Ni–O ₁ –Nb (°)	170.125
Bi–Ba (Å)	0.1649

where λ is the X-ray wavelength, θ is the diffraction angle for the most intense peak (101), and β is defined as $\beta^2 = \beta_m^2 - \beta_s^2$. Here β_m is the experimental full width at half maximum (FWHM), and β_s is the FWHM of a standard silicon sample [35]. The estimated crystallite size of the compound BNO is $D_{SC} = 28.8$ nm. This crystallites size value is less than 100 nm, so the prepared sample can be considered as nanomaterial.

In fact, the Goldschmidt tolerance factor t was calculated [36] and provided by:

$$t = \frac{r_A + r_O}{\sqrt{2}(r_B + r_O)} \quad (2)$$

With $r_A = r(\text{Bi, Ba})$, $r_B = r(\text{Ni, Nb})$ and r_O are the ionic radii associated with the cations of sites A, B and oxygen, respectively. The evolution of crystal structures as a function of the value of the parameter factor are explained below: $0.75 < t < 0.96$: Orthorhombic distortion, $0.96 < t < 0.99$: Rhombohedral distortion and $0.99 < t < 1.06$: Cubic. According to Shannon's ionic radii are: $r(\text{Bi}^{3+}) = 0.96 \text{ \AA}$, $r(\text{Ba}^{2+}) = 1.35 \text{ \AA}$, $r(\text{Ni}^{2+}) = 0.69 \text{ \AA}$, $r(\text{Nb}^{5+}) = 0.64 \text{ \AA}$ and $r(\text{O}^{2-}) = 1.4 \text{ \AA}$ [37, 38]. For our sample, the factor $t = 0.976$ which confirms the rhombohedral system of the material.

3.2 Morphology and chemical composition analysis

To get the grain size and the surface morphology of the sample, we realized their electron micrograph. A scanning electron microscope, with an acceleration voltage that can vary in the range of 0.5–30 kV was used to make the SEM images at a voltage of 21 kV. Figure 2a shows the BNO surface morphology recorded for a gold-plated bulk pellet sample using a scanning electron microscope (SEM). The nature and size of the microstructures of the sample suggest that the surface is very dense due to the uniform grain distribution separated by grain boundaries with different size ranges. From these images, the average grain size obtained is $D_{MEB} = 340$ nm. The average particle size of the material is determined from the size distribution. The grain size estimated from the SEM images is obviously much greater than the one estimated using the Scherrer formula. This distinction is predetermined by the fact that each grain detected

by the SEM is made up of a collection of tiny crystalline grains.

Furthermore, as SEM technique can provide valuable information about the morphology and the external structure of the sample, it can inform us about the chemical composition when it is combined with EDX technology. Figure 2b indicates the corresponding EDX spectra for BNO compound. When energy is absorbed by an atom, the excited electron can fall back to a lower orbital and emit a photon. The EDX spectrum analysis shows the presence of all atoms (Bi, Ba, Ni, Nb and O). The size of this energy is different for each element and divided into K, L and M series. For elements such as Bi, Ba and Nb, the L lines can be used. For nickel atoms, we use the K lines which are clearly visible in the spectrum. The average experimental atomic percentages of the elements calculated from EDX experiment are: Bi% = 7.52, Ba% = 15.13, Ni% = 37.22, Nb% = 16.72 and O% = 21.42, which reveal the purity of the sample.

3.3 Dielectric study

The study of dielectric properties is an important source of information, valid for conduction processes, since it allows determining the origin of dielectric losses, the dipole relaxation time and its activation energy [39]. The complex permittivity of an ideal dielectric is described by the following expression:

$$\varepsilon^*(\omega) = \varepsilon_\infty + \frac{(\varepsilon_s - \varepsilon_\infty)}{\left(1 + \frac{j\omega}{\omega_1}\right)}, \quad (3)$$

where ε_s and ε_∞ : the static permittivity and infinite frequency permittivity. ω_1 : the angular frequency of Debye relaxation.

The behavior of most dielectric materials does not obey the expression; the permittivity is described by a more general expression called the Cole–Cole law [40, 41]:

$$\varepsilon^*(\omega) = \varepsilon_\infty + \frac{(\varepsilon_s - \varepsilon_\infty)}{\left(1 + \frac{j\omega}{\omega_1}\right)} + \frac{\sigma_0}{j\omega\varepsilon_0} \quad (4)$$

Or α : the relaxation time distribution, this is the tilt angle ($\alpha\pi/2$) of the circular arc with respect to the real axis in the plane of permittivity complex, σ_0 : the static conductivity, ω : the frequency, ε_0 : the electrical permittivity of vacuum. Figure 3 illustrates the variation of the real part ε' of the complex permittivity as a function of angular frequency at different

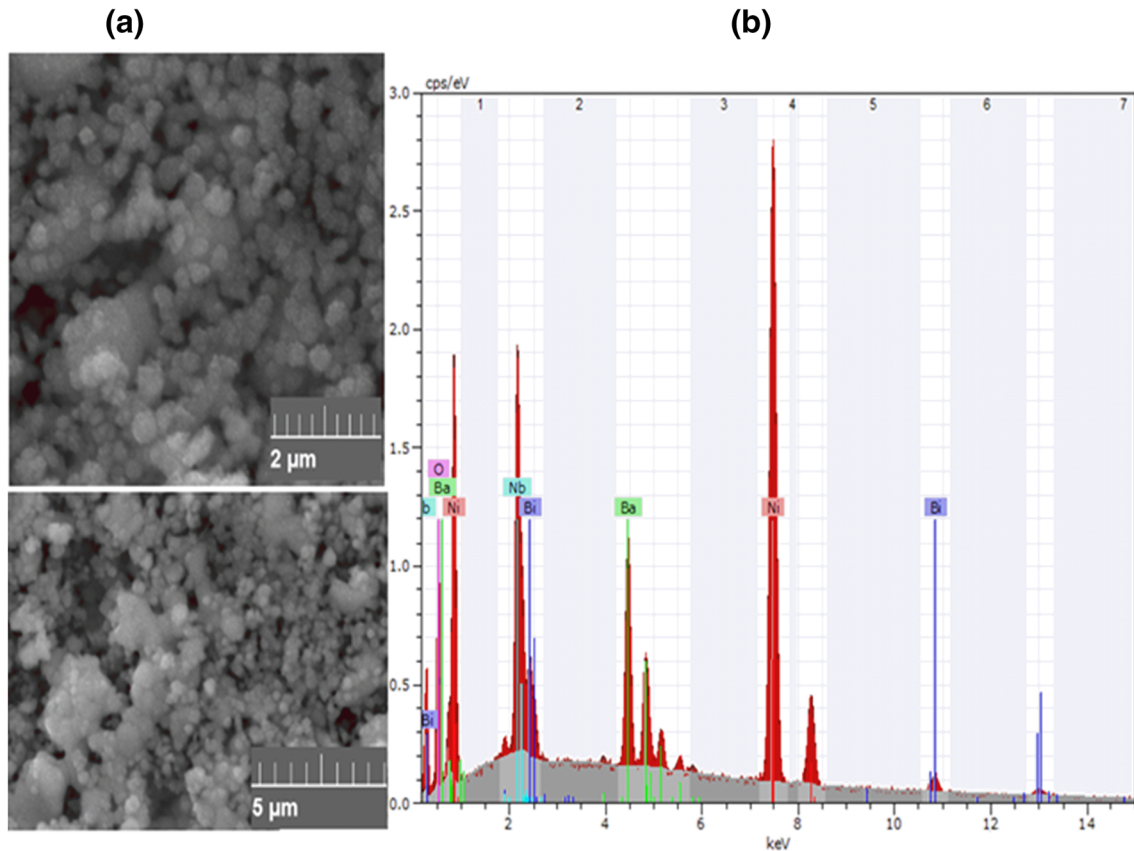


Fig. 2 X-ray powder diffraction of BiBaNiNbO₆ recorded with the Cu K_α radiation

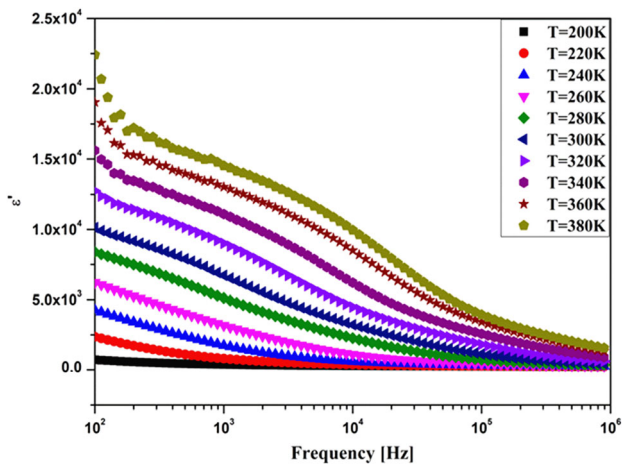


Fig. 3 Frequency variation of the real permittivity part (ϵ') at several temperatures

temperatures of BNO compound. This figure presents two different areas different. A part at other frequencies where we note an increase of the real part with the decrease of the frequency and which represents the process of dielectric relaxation. In this part, the increase of ϵ' represents for low

temperatures the effects of grain boundaries and for high temperatures, the effects of electrodes and grain boundaries. On the other hand, the evolution of the imaginary part is presented in Fig. 4. The spectra of $\epsilon''(\omega)$ show two distinct regions that characterize two

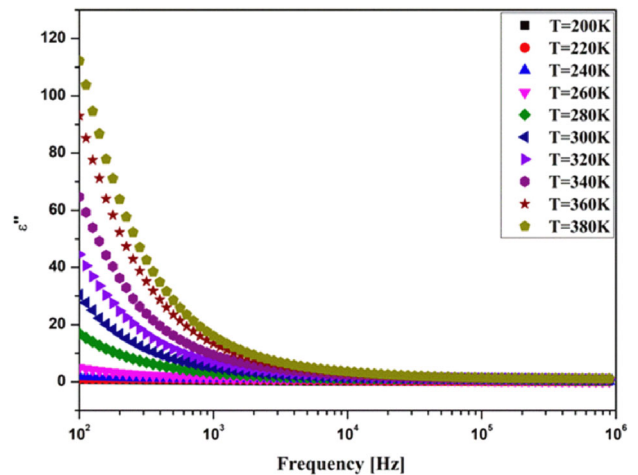


Fig. 4 The frequency dependence of the (ϵ'') at several temperatures of the sample

relaxation processes. The low frequency region characterizes the electrical response related to free carriers while the high frequency region corresponds to a dielectric response.

3.4 Characterization by complex impedance spectroscopy

Impedance spectroscopy has been employed to obtain a detailed analysis about the electrical properties such as dielectric relaxation processes, resistive and conductive behavior in a polycrystalline sample. Based on an equivalent circuit, impedance spectroscopy is a well-known tool to distinguish between grains and grain boundaries of the sample [42]. In order to understand the electrical behavior of the synthesized material, the study of an equivalent electrical circuit is necessary. The electrical measurements of BNO compound was carried out on pellets of 10 mm diameter and 1.32 mm thickness in the temperature range 200–380 K.

To understand the complex mechanism in the low temperature region the variation of Z' with $-Z''$ at different temperatures is shown in Fig. 5. It is clear that the spectra have two arcs of circles: a small one being detected at high frequencies and the other large one at low frequencies. The grain contributions and grain boundaries are represented by these arcs, respectively. Moreover, these arcs are not ideal, which explains this compound adheres to the Cole-Cole model rather than the Debye model [43]. When the temperature increases, we also observe that the

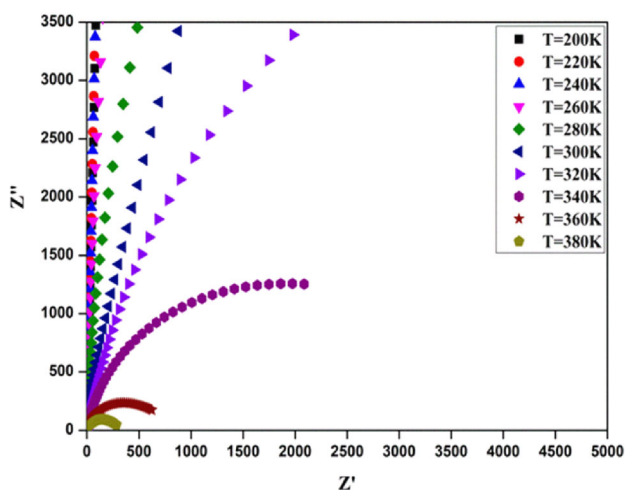


Fig. 5 Impedance diagram of BiBaNiNbO₆ sample at different temperatures

radius of the semicircles shrinks, favoring the semiconductor character of the material and the thermal activation of the conduction processes. It is noticed that the resistance always decreases when the temperature increases. Moreover, the small circle detected at low frequencies corresponds to grain boundaries, while the large circle visible at high frequencies corresponds to grains. The impedance spectra of the material were modeled using Zview software by an equivalent circuit formed by a parallel combination of resistance (R_g -CPE_g) and (R_{gb} -CPE_{gb}) as shown in Fig. 6. The resistances R_g and R_{gb} , respectively describe grain resistance and grain boundaries and fractal capacitances CPE_g and CPE_{gb}.

To account for the depressed semi-circle, C is replaced by constant phase element (CPE) of the circuit and the impedance is expressed as [44]:

$$Z_{\text{CPE}} = \frac{1}{Q(j\omega)^\alpha} \quad (5)$$

The value of the exponent α determines the capacitive nature of the CPE element: if $\alpha = 1$, CPE is an ideal capacitance, if $\alpha = 0$, CPE behaves as a pure resistance, if $\alpha = -1$, CPE behaves like an inductance. The parameters R_g , R_{gb} , α_g and α_{gb} are summarized in Table 2. From the table it has been seen that the resistance values decrease with temperature which is normal for the thermal behavior of the conductivity. The values of the Q_g capacities are of the order of pF, which implies that the half circles observed at high frequencies are essentially due to the response of the grains. For Q_{gb} are of the order of nF showing that the half circles observed at low frequencies are due to the response of the grain boundaries.

Figure 7 shows the variation of the real part of impedance Z' with the frequency at some representative temperatures. At low temperature, the impedance value is typically higher in the low frequency

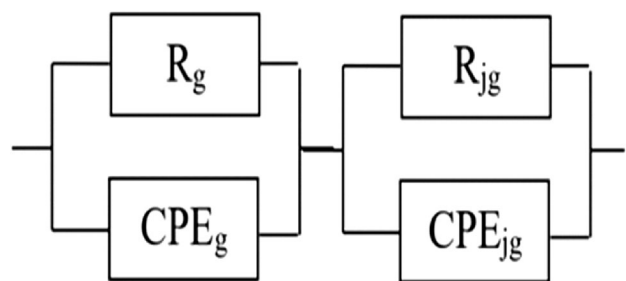


Fig. 6 Electrical equivalent circuit

Table 2 Electrical parameter of the equivalent circuit

T (K)	200	220	240	260	280	300	320	340	360
$R_g (\times 10^5 \Omega)$	8.22	8.06	6.87	5.82	4.60	3.86	2.79	2.41	1.97
Q_g (pF)	33.11	36.45	39.20	41.8	46.32	52.24	56.01	60.13	67.21
α_g	0.778	0.777	0.775	0.769	0.762	0.754	0.749	0.745	0.739
$R_{gb} (\times 10^6 \Omega)$	3.33	2.58	2.14	1.76	1.41	1.03	1.03	0.75	0.56
Q_{gb} (nF)	0.19	0.27	0.31	0.35	0.40	0.42	0.44	0.47	0.51
α_{gb}	0.916	0.873	0.855	0.864	0.842	0.887	0.891	0.922	0.925

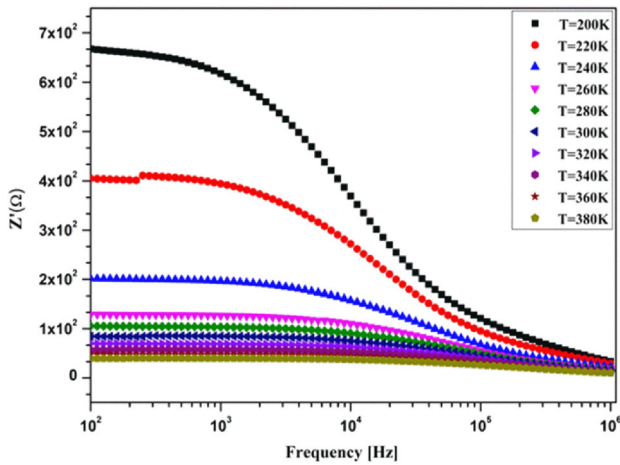


Fig. 7 Variation of the real part of impedance Z' with frequency at different temperatures

region. Then, Z' decreases with increasing temperature and frequency. Such behavior indicates the increase of the ac conductivity. The value of Z' appears to merge in the high frequency region irrespective of the temperature. This result may possibly be related to the release of space charge as a result of reduction in the encountered barrier with rise in temperature. It may be a responsible factor for the enhancement of the material conductance with the temperature at high frequencies. This interpretation was confirmed by the higher impedance values at lower frequencies. The same behavior of Z at lower frequencies was observed by Iben Nassar et al. [20]. Figure 8 illustrates the variation of imaginary part of impedance Z'' with frequency at various temperatures. Each spectrum is characterized by the appearance of a single peak at a relaxation frequency f_{max} , which shifts to higher frequency with increasing temperature. This behavior describes the type and the strength of electrical relaxation phenomenon in the material. A significant broadening of the peaks with increasing in temperature suggests the existence of a temperature-dependent electrical relaxation

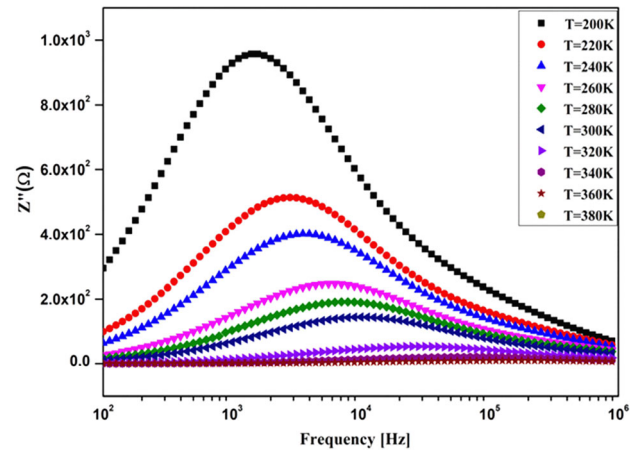


Fig. 8 Variation of the real part of impedance Z'' with frequency at different temperatures

phenomenon. Further, the magnitude of Z'' decreases gradually when the temperature increases. This may be due to an accumulation of electrical charges in the sample. The impedance data have been used to evaluate the relaxation frequency $f_{max} = (1/\tau)$ of the electrical phenomena in the material. The plot of \ln

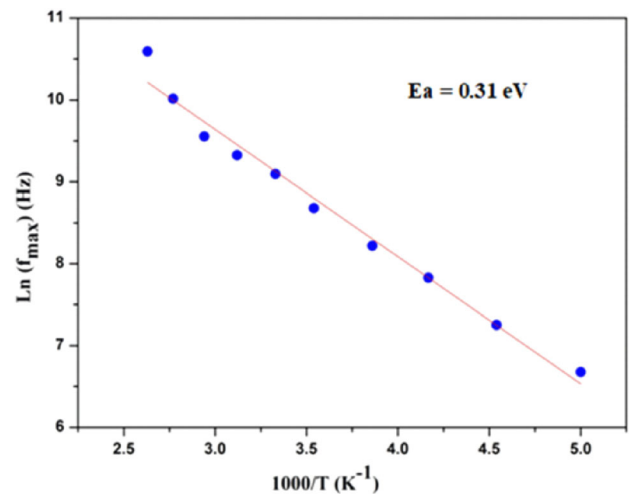


Fig. 9 Variation of $\ln(f_{max})$ as a function of the inverse of temperature

(f_{\max}) versus $1000/T$ presented in the Fig. 9, it can be described by the by Arrhenius plot [45] and is given as:

$$f_{\max} = f_0 \exp\left(\frac{-E_a}{K_B T}\right) \quad (6)$$

With, f_0 is the pre-exponential factor, T is the temperature, E_a is the activation energy and K_B is the Boltzmann constant, is well fitted by a straight line at high temperature, giving an activation energy 0.31 eV.

3.5 Electrical conductivity

In order to analyze the dynamic response of the material as a function of the applied electric field, the study of the experimental data was performed on the conductivity, also called alternating current conductivity (σ_{ac}), this conductivity is associated with the conduction of electric charges whose direction is in phase with the applied electric field and their frequency dependence also provides information on the nature of the charge carriers. The frequency dependence of the conductivity follows by the Jonscher universal power law [46, 47] expressed as:

$$\sigma_{ac}(\omega) = \sigma_{dc} + A\omega^s, \quad (7)$$

where σ_{dc} is the direct current conductivity of the sample and ω is the angular frequency. The exponent n represents the degree of interaction between mobile ions with the lattices around them, and A is a constant which determines the strength of polarizability. The variation of the conductivity as a function of frequency has been investigated in BNO compound. The conductivity spectrum is presented in Fig. 10. We can notice that the ac conductivity spectra can be splitted into two parts. In the first part, an independent frequency behavior of the conductivity in the low frequency region is observed for each temperature. In the second part, which concerns the high frequency region, the conductivity is found to increase with increasing frequency. According to Jonscher [47], the variation of the conductivity with frequency can be due to the relaxation of the ionic atmosphere after the movement of the particle.

The exponent S depends strongly in temperature. Its value has a physical meaning. If $S \leq 1$, the hopping motion involves a translation motion with a sudden hopping [48], whereas if $S \geq 1$, the hopping motion involves localized hopping without the

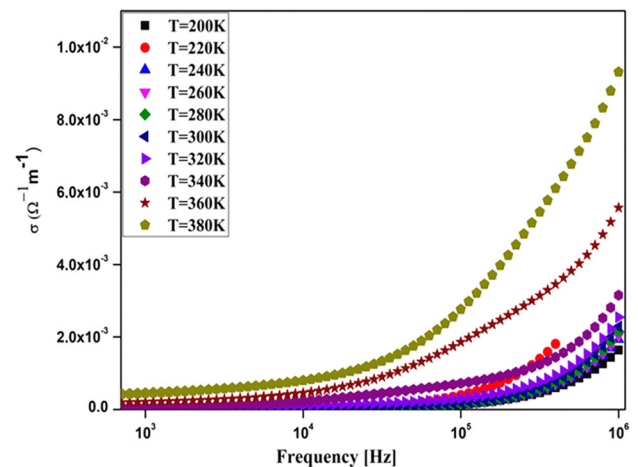


Fig. 10 Variation of conductivity as a function of frequency for BiBaNiNbO₆ at different temperatures

species leaving the neighborhood [49]. Figure 11 shows the thermal variation of S , as determined by the AC conductivity fit. There are several models that can explain the conduction mechanism in materials. We can cite for examples the Quantum Tunnel Effect (QMT) [50, 51] model, the Barrier Correlated Jump model (CBH) [52, 53], the non-overlapping small polaron tunneling model (NSPT) and the tunnel models of the large polaron (OLPT) [54]. According to the figure the exponent s increases with the increase in temperature. So, the most suitable model to characterize the conduction phenomenon in BNO compound is the NSPT model.

In this model, the expression of the exponent S is determined according to the following formula [55]:

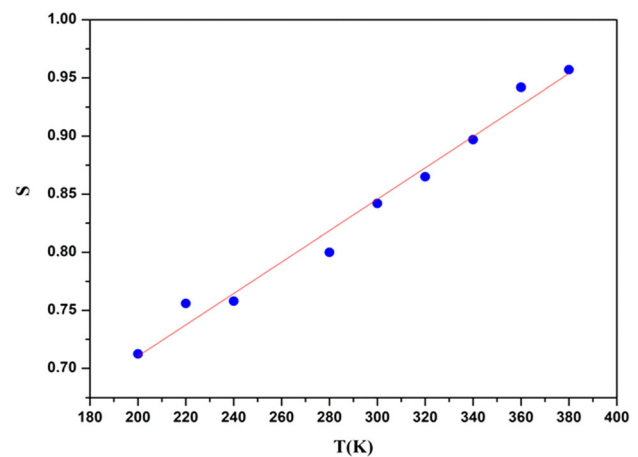


Fig. 11 Temperature dependence of the exponent s

$$S = 1 + \frac{4K_B T}{W_m - K_B T \ln(\omega\tau_0)}, \tag{8}$$

where K_B is the Boltzmann constant, W_m is the binding energy of the charge carrier. If the ratio of $W_m/K_B T$ is large, the exponent s becomes:

$$s = 1 + \frac{4K_B T}{W_m} \tag{9}$$

The conductivity is characterized by an Arrhenius type behavior [56]:

$$\sigma_{DC} = A \exp\left(\frac{-E_a}{K_B T}\right), \tag{10}$$

where T is the temperature, E_a is the activation energy, A is the pre-exponential factor and K_B is the Boltzmann constant ($K_B = 8.617 \times 10^{-5} \text{ eV K}^{-1}$). The temperature dependence of the conductivity $\ln(\sigma_{dc} T)$ vs $1000/T$ as illustrate in Fig. 12.

The activation energy estimated from the slope of the linear fit is about 0.36 eV. Such value indicates that the conduction mechanism for the present system may be due to the polaron hopping based on electron carriers. In addition, it is evident that the values of the activation energy derived from conductivity and the frequency corresponding to the relaxation peaks of the imaginary part of the impedance (Z'') are different, which explains why the process of relation and the mechanism of conduction do not use the same charge carriers.

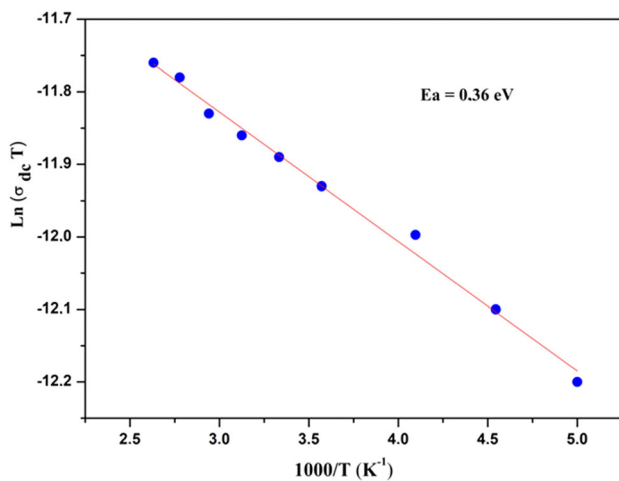


Fig. 12 Variation of $\ln(\sigma_{dc})$ with the inverse of temperature

4 Conclusions

BiBaNiNbO₆ was successfully synthesised by using a sol-gel method. The X-ray diffraction study confirmed that the compound is monophasic. The formed sample was found to crystallise in rhombohedral $R\bar{3}C$ symmetry. The morphological and chemical study were studied using the scanning electron microscope (SEM) and the prepared material presented a dense and uniform morphology with an average particle size equal to 340 nm which is very high compared to crystallite particle size determined from (XRD). Dielectric, impedance and electrical conductivity of the sample were studied in the temperature range 200–380 K and frequency range 100 Hz–1 MHz. The frequency dependence of impedance shows a relaxation phenomenon and semiconductor behavior in the studied material. The Nyquist diagram shows a modular behavior with an equivalent circuit consisting of two circuits in series. One contains constant phase element ($R_g//CPE_g$) and ($R_{gb}//CPE_{gb}$). In addition, the decrease of R_g and R_{gb} with increasing temperature suggests the semiconductor behavior of the sample. On the other hand, the variation of the conductivity has been modeled by the empirical law of Arrhenius and the most adequate conduction model is NSPT. The activation energy obtained for the conductivity and impedance are very close. Hence, good characteristics of dielectric and electrical in this compound were exhibited. It could be used in electrical applications such as capacitors and energy storage.

Author contributions

All authors take public responsibility for the content of the work submitted for review. The contributions of all authors must be described in the following manner: The authors confirm contribution to the paper as follows: study conception and design: KIN and FT; data collection: MS; analysis and interpretation of results: NR and AN; draft manuscript preparation: SST and MPFG. All authors reviewed the results and approved the final version of the manuscript. The author confirms sole responsibility for the following: study conception and design, data collection, analysis and interpretation of results, and manuscript preparation.

Data availability

Data sharing not applicable to this article as no datasets were generated or analyzed during the current study.

Declarations

Conflict of interest The authors declare that no funds, grants, or other support were received during the preparation of this manuscript.

References

- A.S. Bhalla, R. Guo, R. Roy, *Mater. Res. Innov.* **4**, 3–26 (2000)
- E.G. Babakhani, J. Towfighi, L. Shirazi, A. Nakhaeipour, A. Zamaniyan, Z. Shafiei, *J. Mater. Sci. Technol.* **28**, 177 (2012)
- F. Ramezanipour, J.E. Greedan, L.M.D. Cranswick, V. Ovidiu Garlea, R.L. Donaberger, J. Siewenie, *J. Chem. Soc.* **134**, 3215 (2012)
- D.K. Mahato, A. Dutta, T.P. Sinha, *J. Mater. Sci.* **45**, 6757–6762 (2010)
- F.M. Casallas, E. Vera-López, D.A. Landínez Téllez, D.E. Saavedra Mesa, J. Roa-Rojas, *J. Phys.* **480**, 012034 (2014)
- O. Ortiz-Díaz, M.J.A. Rodríguez, F. Fajardo, D.A.L. Tellez, J. Roa-Rojas, *J. Phys. B* **398**, 248 (2007)
- M.A. Mahdi, S.R. Yousefi, L.S. Jasim, M. Salavati-Niasari, *Int. J. Hydrogen Energy* **47**(31), 14319–14330 (2022)
- S.R. Yousefi, H.A. Alshamsi, O. Amiri et al., *J. Mol. Liq.* **337**, 116405 (2021)
- S.R. Yousefi, D. Ghanbari, M. Salavati-Niasari et al., *J. Mater. Sci.: Mater. Electron.* **27**(2), 1244–1253 (2016)
- S.R. Yousefi, M. Ghanbari, O. Amiri et al., *J. Am. Ceram. Soc.* **104**(7), 2952–2965 (2021)
- S.R. Yousefi, A. Sobhani, H.A. Alshamsi et al., *RSC Adv.* **11**(19), 11500–11512 (2021)
- S.R. Yousefi, O. Amiri, M. Salavati-Niasari, *Ultrason. Sonochem.* **58**, 104619 (2019)
- Y.-H. Huang, R.I. Dass, Z.-L. Xing, J.B. Goodenough, *Science* **312**, 254–257 (2006)
- W. Zhang, M. Anaya, G. Lozano, M.E. Calvo, M.B. Johnston, H. Míguez, H.J. Snaith, *Nano Lett.* **15**(3), 1698 (2015)
- S.R. Yousefi, A. Sobhani, M. Salavati-Niasari, *Adv. Powder Technol.* **28**(4), 1258–1262 (2017)
- S.R. Yousefi, D. Ghanbari, M. Salavati-Niasari, M. Hassani-pour, *J Mater Sci Mater Electron.* **27**(2), 1244–1253 (2016)
- K. Iben Nassar, N. Rammeh, S.S. Teixeira, M.P.F. Graça, *J. Electron. Mater.* **51**, 370–377 (2022)
- M. Mohamed, K. Iben Nassar, M. Mohamed, N. Rammeh, M.P.F. Graça, *J. Mol. Struct.* **1258**, 132658 (2022)
- K. Iben Nassar, M. Slimi, N. Rammeh, S.S. Teixeira, M.P.F. Graça, *Appl. Phys. A* **127**, 940 (2021)
- K. Iben Nassar, M. Slimi, N. Rammeh, A. Bouhamed, A. Njeh, O. Kanoun, *J. Mater. Sci.: Mater. Electron.* **32**, 24050–24057 (2021)
- N. Moreno, L. Barbosa, D.R. Ardila, J.P. Andreetta, *J. Supercond. Nov. Magn.* **26**, 2501–2503 (2013)
- R. Borges, R. Thomas, C. Cullinan, J. Coey, R. Suryanarayanan, L. Ben-Dor, L. Pinsard-Gaudart, A. Revcolevschi, *J. Phys.: Condens. Matter* **11**, L445 (1999)
- W.E. Pickett, D.J. Singh, *Phys. Rev. B* **53**, 1146 (1996)
- K.-I. Kobayashi, T. Kimura, H. Sawada, K. Terakura, Y. Tokura, *Nature* **395**, 677 (1998)
- N.A. Benedek, C.J. Fennie, *J. Phys. Chem. C* **117**, 13339 (2013)
- M. Li, M.J. Pietrowski, R.A. De Souza, H. Zhang, I.M. Reaney, S.N. Cook et al., *Nat. Mater.* **13**, 31–5 (2014)
- A. Manohar, C. Krishnamoorthi, *J. Alloys Compd.* **722**, 818–827 (2017)
- A. Manohar, C. Krishnamoorthi, *J. Photochem. Photobiol. B* **177**, 95–104 (2017)
- A. Manohar, C. Krishnamoorthi, *J. Mater. Sci.: Mater. Electron.* **29**(1), 737–745 (2018)
- A. Manohar, C. Krishnamoorthi, K.C.B.B. Naidu et al., *Appl. Phys. A* **125**(7), 1–10 (2019)
- A. Manohar, V. Vijayakanth, S.V.P. Vattikuti et al., *Mater. Chem. Phys.* **286**, 126117 (2022)
- A. Manohar, V. Vijayakanth, K.H. Kim, *J. Alloys Compd.* **886**, 161276 (2021)
- A. Manohar, V. Vijayakanth, R. Hong, *J. Mater. Sci.: Mater. Electron.* **31**(1), 799–806 (2020)
- A. Manohar, C. Krishnamoorthi, *J. Magn. Magn. Mater.* **443**, 267–274 (2017)
- A. Guinier, *Théorie et technique de la Radiocristallographie*, 3rd edn. (Dunod, Paris, 1964), p.462
- V.M. Goldschmidt, *Geochemische Verteilungsgesetze der Element VII, VIII (1927/1928)*
- R.D. Shannon, *Acta Cryst. A* **32**, 751 (1976)
- M.D. Ingram, *Phys. Chem. Glass.* **28**, 215 (1987)
- H. Kolodziej, L. Sobczyk, *Acta Phys. Pol. A* **39**, 59 (1971)
- N. Zouari, H. Khemakhem, M. Gargouri, M. Mnif, T. Mhiri, A. Daoud, *Phys. Status Solidi B* **213**, 219 (1999)
- S. Nasri, M. Megdiche, M. Gargouri, K. Guidara, *Ionics* **20**, 399–407 (2014)
- P. Thongbai, S. Tangwancharoen, T. Yamwong, S. Maensiri, *J. Phys.: Condens. Matter* **20**, 395227–395238 (2008)
- S.K. Barik, R.N.P. Choudhary, P.K. Mahapatra, *Appl. Phys. A* **88**, 217–222 (2007)

44. A. Leonide, V. Sonn, A. Weber, E. Ivers-Tiffée, J. Electrochem. Soc. **155**, B36–B41 (2008)
45. M.D. Migahed, N.A. Bakr, M.I. Abdel-Hamid, O. EL-Hannafy, M. El-Nimr, J. Appl. Polym. Sci. **59**, 655–662 (1996)
46. S. Lanfredi, P.S. Saia, R. Lebullenger, A.C. Hernandez, Solid State Ion. **146**, 329 (2002)
47. A.K. Jonscher, *Universal Relaxation Law: A Sequel to Dielectric Relaxation in Solids* (Chelsea Dielectric Press, London, 1996)
48. A. Pelaiz-Barranco, M.P. Gutierrez-Amador, A. Huanosta, R. Valenzuela, Appl. Phys. Lett. **73**, 2039 (1998)
49. P. Banerji Behera, R.N.P. Nayak, J. Choudhary, J. Alloys Compd. **436**, 226 (2007)
50. X. Lecleac'H, Physics **40**, 27 (1979)
51. A. Ghosh, Phys. Rev. B **42**, 5665 (1990)
52. K. Shimakawa, Philos. Mag. B **46**, 123 (1982)
53. S.R. Elliott, Philos. Mag. B **36**, 129 (1978)
54. J.T. Gudmundsson, H.G. Svavarsson, S. Gudjonsson, H.P. Gislason, J. Phys. B **340**, 324–328 (2003)
55. S.R. Elliot, Adv. Phys. **36**, 135–217 (1987)
56. K.P. Padmasree, D.K. Kanchan, A.R. Kulkarni, Solid State Ion. **177**, 475 (2006)

Publisher's Note Springer Nature remains neutral with regard to jurisdictional claims in published maps and institutional affiliations.

Springer Nature or its licensor (e.g. a society or other partner) holds exclusive rights to this article under a publishing agreement with the author(s) or other rightsholder(s); author self-archiving of the accepted manuscript version of this article is solely governed by the terms of such publishing agreement and applicable law.